

Hadron Spectroscopy with Dynamical Chirally Improved Fermions

Christof Gattringer,¹ Christian Hagen,² C. B. Lang,¹
 Markus Limmer,¹ Daniel Mohler,¹ and Andreas Schäfer²

(BGR [Bern-Graz-Regensburg] Collaboration)

¹*Institut für Physik, FB Theoretische Physik, Universität Graz, A-8010 Graz, Austria*

²*Institut für Theoretische Physik, Universität Regensburg, D-93040 Regensburg, Germany*

(Dated: December 9, 2008)

We simulate two dynamical, mass degenerate light quarks on $16^3 \times 32$ lattices with a spatial extent of 2.4 fm using the Chirally Improved Dirac operator. The simulation method, the implementation of the action and signals of equilibration are discussed in detail. Based on the eigenvalues of the Dirac operator we discuss some qualitative features of our approach. Results for ground state masses of pseudoscalar and vector mesons as well as for the nucleon and delta baryons are presented.

PACS numbers: 11.15.Ha, 12.38.Gc

Keywords: Hadron spectroscopy, dynamical fermions

I. INTRODUCTION

Lattice Dirac operators that obey the so-called Ginsparg-Wilson (GW) relation [1] implement a lattice version of the chiral symmetry transformations [2]. Presently only one explicit formulation of lattice fermions, the overlap Dirac operator [3, 4], is GW exact in that sense. There are, however, several formulations approaching GW exactness in various ways. Among them is the domain-wall formulation [5, 6], which approaches the overlap operator in the limit of infinite extent of an artificial 5-th dimension. Another one is the so-called perfect Dirac operator [7, 8], which if constructed explicitly, would obey the GW condition, and which has been approximated by a parameterized fixed-point form. Here we discuss a simulation with the so-called Chirally Improved (CI) Dirac operator [9, 10], which is also a parameterization of a Dirac operator obeying the GW relation approximately.

Advantages of GW exact fermions are that there is no additive mass renormalization and thus no spurious zero modes at non-zero quark masses. Operators are protected by chiral symmetry which is convenient for the determination of certain matrix elements. Technically the GW exact overlap operator involves taking the square root of a simpler kernel operator (e.g., the Wilson operator), which is computationally roughly two orders of magnitude more expensive than simulations with non-GW-operators. This is not only due to the technical implementation (through, e.g., polynomial series or rational functions) but also due to tunneling problems between sectors of different topology. Therefore, only a few groups have attempted to implement dynamical overlap fermions [11, 12, 13, 14, 15, 16, 17, 18, 19, 20, 21, 22].

On the other hand, GW-type operators, fulfilling the GW condition in some approximation, although more expensive than simple Wilson-Dirac operators, have been studied in quenched calculations within the BGR collaboration for some time. There we demonstrated that at least for baryon masses the $\mathcal{O}(a^2)$ corrections are quite small [23] and that field renormalization constants behave almost like in the chirally symmetric case [24]. Motivated by these results we have started to implement CI fermions for a dynamical simulation on smaller lattices [25] and are now presenting details and results of our simulations on larger lattices.

First results involving dynamical CI fermions on $16^3 \times 32$ lattices were published in [26, 27], and results for smaller lattices can be found in [25, 28]. In this paper we concentrate on technical

aspects of the simulation and present first results for the hadron mass spectrum for three sets of parameters, corresponding to three different pion masses, giving an overview of the current project status. We start with an explanation of all the technicalities, i.e., simulation details and equilibration behavior, followed by the first analysis results for ground state masses of mesons and baryons. We finish with a discussion of the results and a summary.

II. SETUP AND SIMULATION

A. CI Dirac operator and action

For the fermions we use the so-called Chirally Improved (CI) Dirac operator D_{CI} [9, 10]. It obeys chiral symmetry only approximately, depending on the truncation in the extent of the interaction terms. Plugging a general ansatz into the Ginsparg-Wilson equation leads to a set of algebraic equations for the coefficients, which can be solved to obtain D_{CI} . The paths and coefficients used in our simulation are given in Appendix A 1. Whereas in the quenched simulations the D_{CI} coefficients were adapted to the values of the gauge coupling such as to have (almost) no mass renormalization, we now decided to use the same D_{CI} parameters for all dynamical runs. This implies an additive mass renormalization, i.e., the “mass parameter” m_0 does not give the bare mass directly. We adjust the value of m_0 such as to get suitable PCAC masses (also called AWI-masses since their definition comes from the axial Ward identity). The numbers will be discussed in more detail below.

It was shown in a quenched calculation using D_{CI} [10], that the Lüscher-Weisz gauge action [29] produces smoother gauge configurations than the Wilson gauge action, and thus is used in our simulation. For completeness we also list details of the gauge action in Appendix A 2.

Another important ingredient in our simulation is smearing, since the smearing procedure results in better chiral properties of the operator, as can be seen from the eigenvalue spectrum of the Dirac operator [30]. In earlier quenched studies with D_{CI} so-called HYP smearing [31] was applied. Since such a smearing procedure is not differentiable and thus not well suited for Hybrid Monte-Carlo simulations, we decided to use the “differentiable” stout-smearing [32]. In our simulation we have been using one level of stout-smearing, such that the value of the plaquette is maximized. The stout smearing is considered to be part of the definition of the full Dirac operator.

More recently, other suggestions for efficient differentiable smearing methods have been published [33, 34]. For consistency we continued to use the stout type smearing with which we started our study.

B. Run parameters

For the simulation presented here we use lattices of size $16^3 \times 32$ at three different values of the gauge coupling β_1 and the bare mass parameter m_0 , all of which can be found in Tab. I. The physical volume is always ~ 2.4 fm. The pion mass ranges from approximately 530 MeV down to 320 MeV. The total number of gauge configurations produced, N_{conf} , can also be found in Tab. I.

C. Algorithm

The algorithm we use for generating our gauge configurations is a Hybrid Monte-Carlo (HMC) [35] algorithm plus some additional features. HMC seems to be the most suitable algorithm for our goal.

Run	m_0	β_1	β_2	β_3	m_{HB}	N_{conf}	P_{acc}
A	-0.050	4.70	-0.3941	-0.06063	$\sqrt{0.03}$	100	0.904
B	-0.060	4.65	-0.3899	-0.05998	$\sqrt{0.02}$	200	0.911
C	-0.077	4.58	-0.3841	-0.05908	$\sqrt{0.02}$	200	0.858

TABLE I: The parameters for the different runs. The number of pseudofermions $N_{\text{PF}} = 2$, the total length of the trajectories is 1 in HMC time units. In the 6-th column the parameter for the Hasenbusch mass preconditioning is given (see Sect. II C for more details).

For the HMC we need a generalization of the Hamiltonian evolution for a system of classical mechanics in a fictitious HMC time to our system of fields $U_{n,\mu}$. For that purpose we introduce traceless hermitian matrices $P_{n,\mu} \in \mathfrak{su}(3)$ which act as conjugate momenta for the $U_{n,\mu}$, with n, μ being the lattice site and the direction of the link, respectively. We now can define the time derivative of $U_{n,\mu}$ as

$$\dot{U}_{n,\mu} = i P_{n,\mu} U_{n,\mu}. \quad (1)$$

Then, a Hamiltonian H can be defined as

$$H = \frac{1}{2} \sum_{n,\mu} \text{Tr} (P_{n,\mu}^2) + S_{\text{g}} + \phi^\dagger (D^\dagger D)^{-1} \phi, \quad (2)$$

where S_{g} denotes the gauge action and ϕ is the pseudofermion field. The equation of motion for P is obtained via the relation $\dot{H} = 0$,

$$\dot{H} = \sum_{n,\mu} \text{Tr} (P_{n,\mu} \dot{P}_{n,\mu}) + \dot{S}_{\text{g}} + \phi^\dagger \frac{d}{dt} (D^\dagger D)^{-1} \phi = 0, \quad (3)$$

which gives the evolution equation in HMC time $\dot{P} = f(U, \dot{U}, P)$. Evaluating this function for, e.g., Wilson or staggered quarks is not complicated since such types of quarks involve only one link field $U_{n,\mu}$ connecting neighboring sites. In our case, however, paths up to length four, coming from D_{CI} , have to be considered. A more detailed description of the procedure can be found in [36]. For the evolution in HMC time we used the reversible and area preserving leapfrog integration scheme.

To be able to go to smaller quark masses we utilize Hasenbusch mass preconditioning [37]. The basic idea is to split the pseudofermion action into two (or more) parts, separating the small and the large eigenvalues of the Dirac matrix. In our case we always use two pseudofermions. The parameter m_{HB} , which amounts to an additional mass, is deduced from an educated guess [36]. Using N_{PF} pseudofermions, the mass shift is given by

$$m_{\text{HB}}^{(i)} = \begin{cases} (2^{N_{\text{PF}}-i} \lambda_{\min}^i)^{1/N_{\text{PF}}} & , 1 \leq i < N_{\text{PF}} \\ 0 & , i = N_{\text{PF}} \end{cases}. \quad (4)$$

Here, λ_{\min} is the assumed smallest eigenvalue of the Dirac matrix.

For the inversion of $D^\dagger D$ we use the standard conjugate gradient (CG) inverter. These inversions take by far most of the computer time. Thus, several attempts were made to increase the performance of this part of our code. First of all we use a chronological inverter by minimal residue extrapolation [38], taking into account 12 previous solutions. In Fig. 1 we plot the number of conjugate gradient iterations against the leapfrog step i_{LF} . What we see is a rapid decrease in

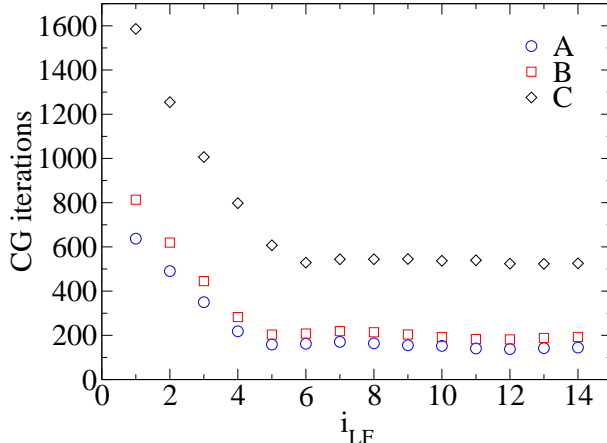


FIG. 1: The average number of needed conjugate gradient iterations is plotted against the first leapfrog steps for each run.

the CG iteration number when more previous solutions become available. However, we find that a plateau is reached already at $i_{LF} = 5$. The overhead caused by the 8 additional matrix vector multiplications is negligible, however.

In a recent paper [39] Dürr et al. presented a mixed precision inverter for the Dirac matrix. In order to ensure reversibility in the molecular dynamics (MD) evolution one should work with double precision accuracy. The method suggested there allows to iteratively improve the inversion accuracy, working partly with single precision and thus faster arithmetic. We choose a final accuracy of $\varepsilon = 10^{-7}$. The gain in run-time per gauge configuration was, e.g., about 33% for run C.

D. Autocorrelation time

A measure for the statistical efficiency of an observable O is the integrated autocorrelation time τ_{int} , defined by

$$\tau_{\text{int}} = \frac{1}{2} + \sum_{t=1}^{\infty} \frac{\Gamma(t)}{\Gamma(0)}, \quad (5)$$

where the autocorrelation function Γ is given by

$$\Gamma(t) = \left\langle (O(t_0) - \langle O \rangle)(O(t_0 + t) - \langle O \rangle) \right\rangle. \quad (6)$$

In practice, the sum (5) has to be truncated at some upper value t_{max} , which we choose at that point where the autocorrelation data becomes noisy. We discuss several observables to be able to figure out the point of equilibration and the statistical independence of our measurements.

On the l.h.s. of Fig. 2 we plot the plaquette values for the three runs. One can clearly see that the runs A and B, starting from “cool” quenched configurations, are equilibrated after roughly $\mathcal{O}(100)$ configurations. Run C does not show a significant equilibration process for the following reason. We started from a configuration B and slowly changed the parameters β_1 and m_0 to the values of run C. This was the starting configuration of the new run sequence C.

Another indicator of equilibrium behavior is the number of CG-steps in the final accept/reject step of the MD evolution, N_{inv} . We show these numbers on the r.h.s. of Fig. 2. Here one can also

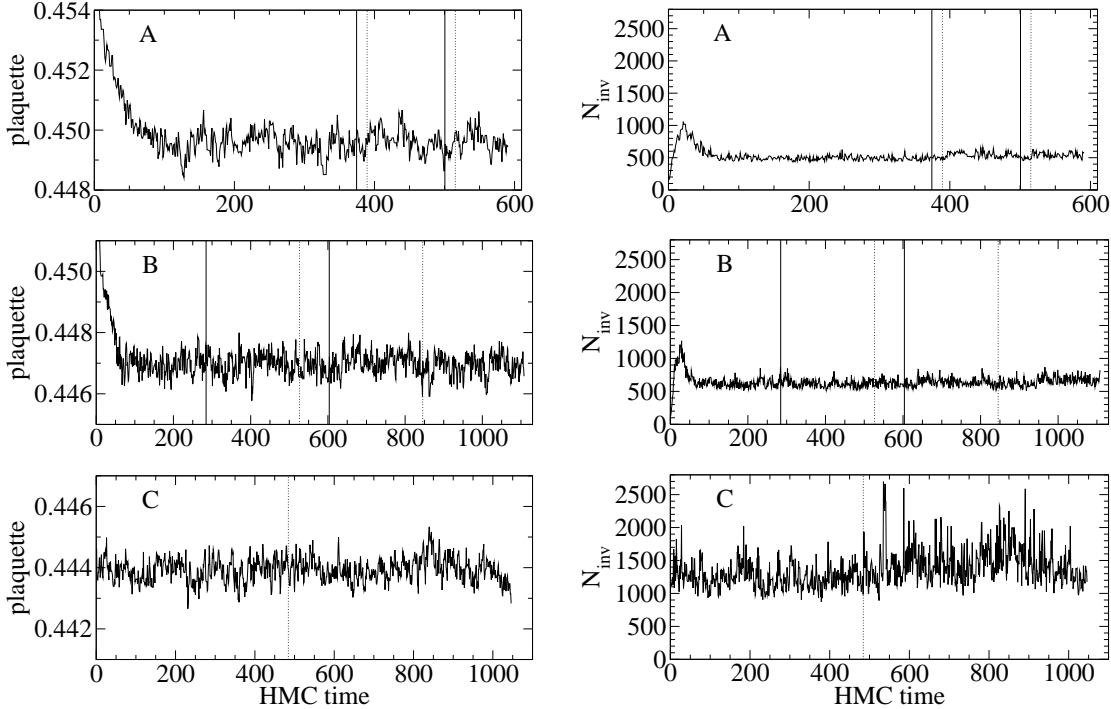


FIG. 2: L.h.s.: The spatially averaged plaquette against the HMC time, from top to bottom we plot runs A, B and C. The dashed line in the plots indicate a change in the algorithm: From that point on we changed to the mixed precision inverter and used Hasenbusch mass preconditioning. In run C the Hasenbusch mass preconditioning was used from the beginning, we only changed to the mixed precision inverter. The full lines in run A and run B indicate a split in the particular run into two separate trajectories to increase the production of gauge configurations per (real) time. R.h.s.: The number of CG iterations, N_{inv} in the accept/reject step, notation like l.h.s.

Run	N_{equi}	$\tau_{\text{int}}(\text{plaq.})$	$\tau_{\text{int}}(N_{\text{inv}})$
A	100	3.5	4.2
B	115	2.4	2.7
C	50	3.7	3.6

TABLE II: Integrated autocorrelation times for the three runs. N_{equi} is the number of configurations skipped after the start.

see that the runs are equilibrated after the above mentioned number of HMC updates. Based on these observations, in our analysis we discarded the first 100, 115, and 50 configurations for runs A, B, and C, respectively.

Starting thus with the equilibrated configuration, we computed the integrated autocorrelation time τ_{int} for the plaquette values and for N_{inv} . The resulting numbers are given in Tab. II and are all below 5. Therefrom we decided to analyze every 5-th configuration, i.e., configurations separated by 5 units of HMC time.

In Fig. 3 we show the history of the pion mass, calculated separately for each analyzed configuration. Details of the used pion interpolator are discussed in the spectroscopy section. No noticeable correlation can be found in the plots.

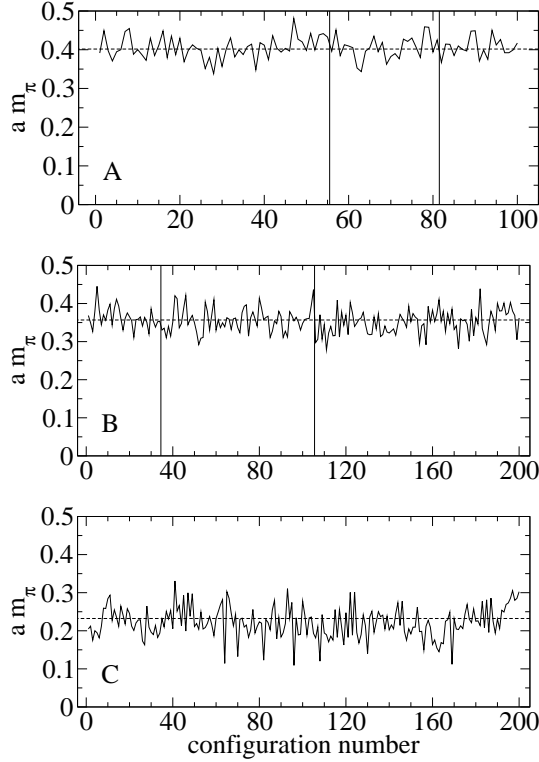


FIG. 3: Time histories of the pion mass determined from single configurations using the interpolator $\bar{u}_w \gamma_5 d_w$ (see Sect. IV C). The horizontal dashed line indicates the mass value obtained from fits to the ww propagators in the range $t = 4 - 15$ (run A, B) or $t = 5 - 15$ (run C). The vertical lines in runs A and B indicate a split into separate sequences such as to enhance statistics by parallel runs.

E. The change in the Hamiltonian

Since we introduced the conjugate momenta P , we describe a microcanonical ensemble of a classical system with a Hamiltonian H . For exact solutions of the equations of motion (MD equations) the Hamiltonian would be a constant of motion and the configurations all would lie on a surface of constant energy. Thus, each created configuration would be accepted. However, due to the discretization with an MD time step δ_t numerical errors are introduced and the Hamiltonian energy is not invariant. We denote the change as ΔH . Each calculated gauge configuration is then accepted with a probability $e^{-\Delta H}$. The area preserving property of MD leads to an inequality [40],

$$e^{\langle -\Delta H \rangle} \leq \langle e^{-\Delta H} \rangle = 1 . \quad (7)$$

Due to this inequality $\langle \Delta H \rangle$ has to be positive and this is indeed the case in our simulations (cf. Tab. III and Fig. 4 for our values). For run B we have a quite large value of $\langle \Delta H \rangle$, coming from a huge spike in ΔH in configuration 730 which is of the order of $\mathcal{O}(10^5)$ bigger than the rest. Also in run C we have a spike at configuration 850, being about $\mathcal{O}(10^3)$ bigger than the other values. Such spikes have already been observed in other simulations with dynamical fermions [13, 41]. Two possible reasons can cause such a spike. One is the instability of HMC for large step sizes in the MD evolution, cf. Ref. [42]. The other one, and this is most likely the case here, is that the Dirac operator can develop very small eigenvalues which lead to these spikes in the derivative of the action.

Run	$\langle \Delta H \rangle$	$e^{-\langle \Delta H \rangle}$	$\langle e^{-\Delta H} \rangle$
A	0.038(11)	0.963	0.989(11)
B	2.01(1.95)	0.134	0.986(10)
B'	0.055(10)	0.947	0.988(10)
C	0.089(59)	0.915	1.034(12)

TABLE III: Averages of ΔH and their exponentials for each run. We only included the equilibrated configurations in our calculations. The 3-rd row contains the data of run B without including configuration 730, which is responsible for the spike in ΔH .

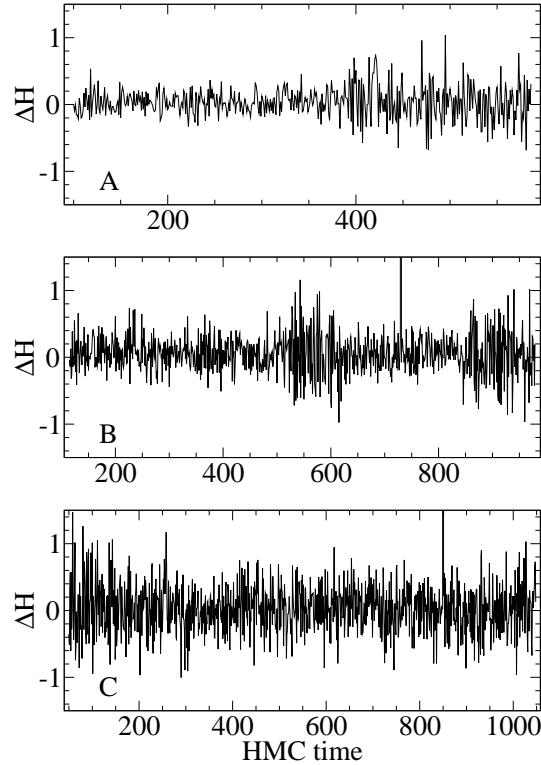


FIG. 4: We plot ΔH against the HMC time starting from the point of equilibration (runs A, B and C are ordered from top to bottom).

We want to conclude with a remark on the relation between ΔH and the acceptance rate. In Fig. 5 we plot the acceptance rate against the averaged ΔH . In our case, at least run A and run C are lying (within error bars) on the predicted curve [43],

$$P_{\text{acc}} = \text{erfc} \left(\frac{\sqrt{\Delta H}}{2} \right) , \quad (8)$$

where erfc is the complementary error function.

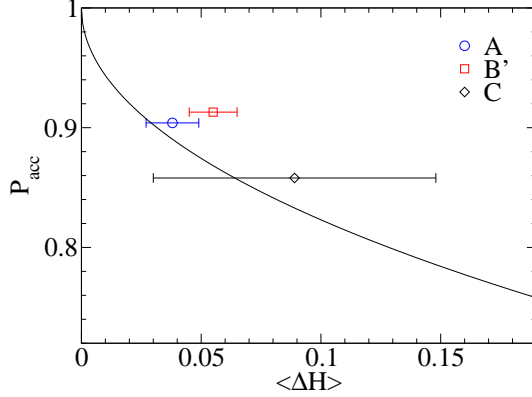


FIG. 5: P_{acc} vs. $\langle \Delta H \rangle$. The black line corresponds to $\text{erfc}(\sqrt{\Delta H}/2)$.

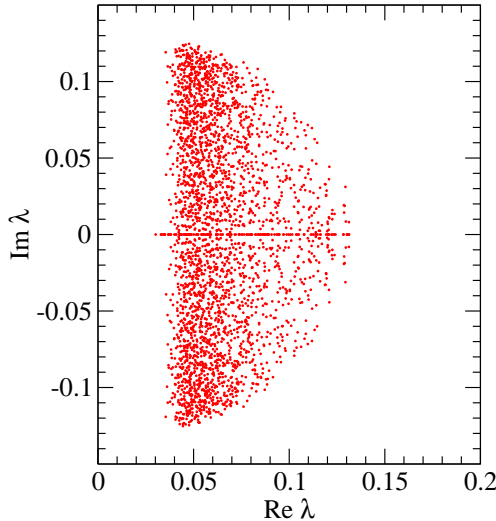


FIG. 6: The smallest 150 eigenvalues superimposed for 20% of the configurations of run A.

F. Dirac eigenvalues

An indicator of the “GW quality” of the Dirac operator is its eigenvalue distribution in the complex plane. Whereas Dirac operators obeying the GW condition in its simplest form have eigenvalues on a unit circle centered at 1, approximate GW operators like D_{CI} deviate from that simple shape showing some scattering of the eigenvalues. Figure 6 shows the (in absolute value) smallest 150 eigenvalues superimposed for 20% of the configurations of run A. Obviously the fluctuation is predominantly towards values inside the unit circle and so-called exceptional configurations (exceptionally small eigenvalues) are suppressed.

Figure 7 shows histograms for the smallest values of purely real λ and for the minimal $\text{Re}(\lambda)$ for all three parameter sets. Both types of histograms give an indication on the permissible values of the smallest quark mass we may obtain for that action, lattice spacing and lattice size. Concerning exceptional configurations, we find a mass gap indicating that we are in a safe region of parameter values.

Several observations can be made from the eigenvalue distributions. Low lying eigenvalues are

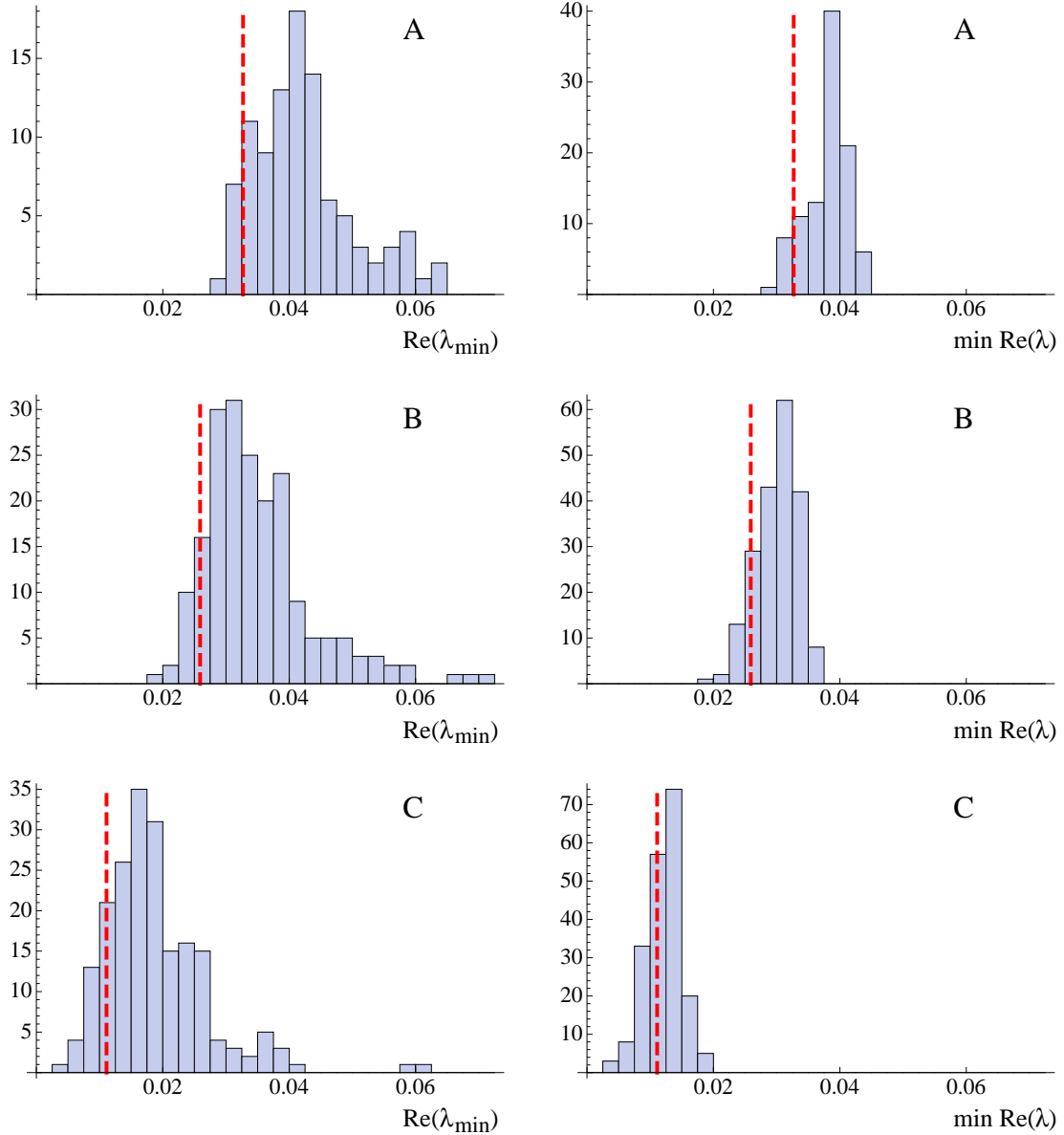


FIG. 7: Histograms for the smallest values of real λ (left) and the smallest values of $\text{Re}(\lambda)$ (right) for parameter sets A-C (from top to bottom). The measured AWI-mass (in lattice units) is indicated by the vertical, dashed line.

depleted as expected for dynamical fermions due to the effect of the determinant in the measure. The boundary close to the circular shape is rather sharp towards larger values of $|\lambda - 1|$. This allows to simulate smaller pion masses on coarse lattices.

The distribution density towards the inner region is, for a given scale parameter, narrower than that for the Wilson action but not as close to the boundary as for quenched simulations with D_{CI} [10].

In the quenched simulation hypercubic smearing was used whereas for the dynamical simulation we apply stout smearing. This latter type of smearing has a weaker smoothing effect than the hypercubic type. We could have applied several subsequent stout smearing steps instead, but we

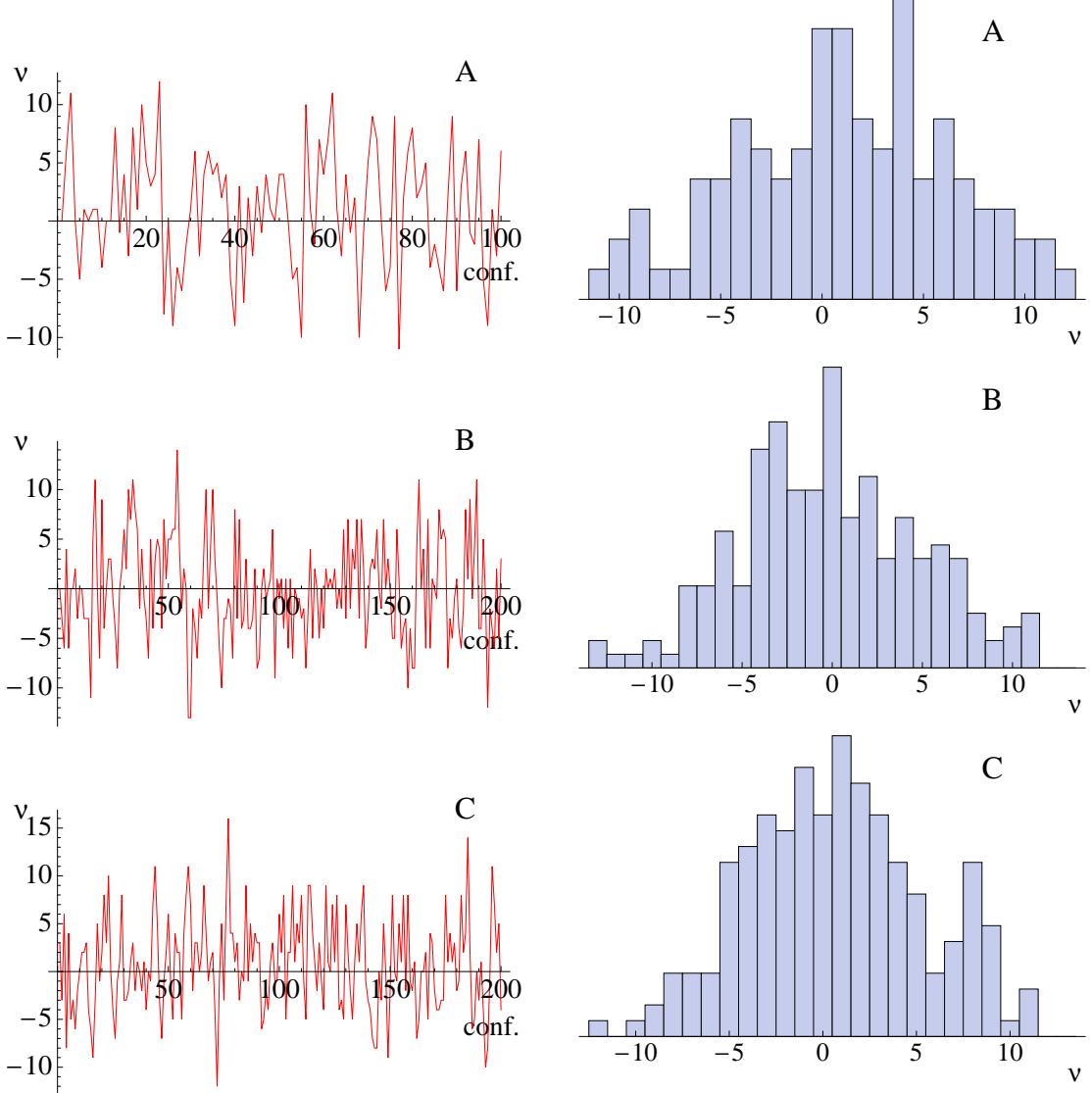


FIG. 8: History of the topology sector ν and corresponding distribution histogram for parameter sets A-C (from top to bottom)

did not want to change the effective action in the middle of our runs. Also, for the quenched ensembles we optimized the action parameters for each value of β_1 . In the dynamical simulation we stayed with the same parameterization of the D_{CI} (except for the bare ‘‘mass’’ parameter m_0) in order to be able to qualitatively compare different runs.

The number of exactly real modes ν , counted according to their chirality $\langle \psi | \gamma_5 | \psi \rangle$, may be related to the topological charge via the Atiyah-Singer index theorem [44]. Although we cannot exclude that we miss some of the inner real modes (cf., Fig. 7), we still get some information on the tunneling between topological sectors from this quantity. Figure 8 demonstrates frequent tunneling and consistency with a Gaussian-like shape of the distribution.

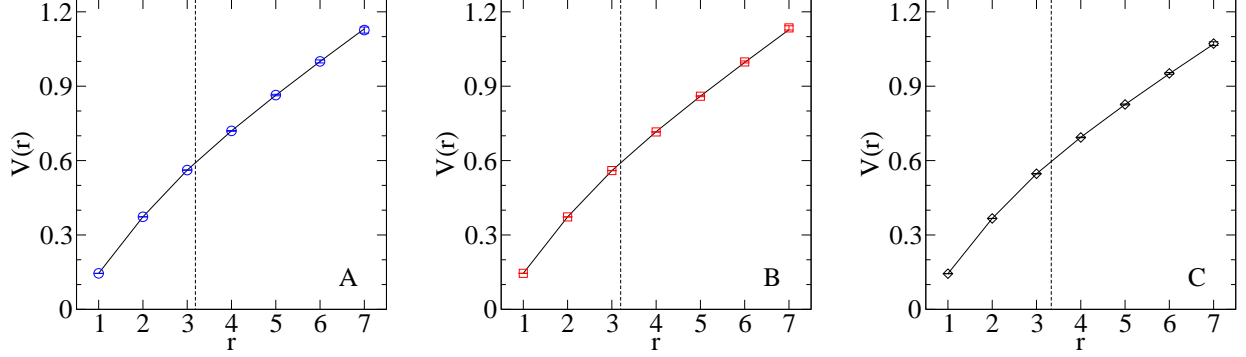


FIG. 9: Fits to the potential in the range $1 \leq r \leq 7$ (symbols represent data points, whereas full black lines are fits to these points). The dashed black line in each plot indicates the distance r in lattice units where Eq. (11) holds.

III. RESULTS FOR LOW ENERGY PARAMETERS

A. Setting the scale

For the determination of the lattice spacing we used the Sommer parameter [45], determined by the lattice potential, which was derived from Wilson loops $W(r, t)$. For improving the signal the gauge configurations have been smeared with hypercubic blocking [31] with parameter values $a_1 = 0.75$, $a_2 = 0.6$ and $a_3 = 0.3$.

We have extracted the potential $V(r)$ for each value of r from linear fits to $\ln W(r, t)$ in the range $4 \leq t \leq 7$. The potential was then fitted in the range $1 \leq r \leq 7$ to

$$V(r) = A + \frac{B}{r} + \sigma r + C \Delta V(r) \quad \text{with} \quad \Delta V(r) \equiv \left[\frac{1}{r} \right] - \frac{1}{r} \quad (9)$$

(all quantities given in lattice units). The perturbative lattice Coulomb potential $[1/r]$ serves as a correction to the continuum Coulomb potential as discussed in [46, 47, 48, 49]. It has been used in the form corrected for hypercubic blocking [50, 51],

$$\left[\frac{1}{r} \right] = \pi \int_{-\pi}^{\pi} \frac{d^3 k}{(2\pi)^3} \frac{\cos(\mathbf{k} \cdot \mathbf{r}) \cdot S_{\text{HYP}}(\mathbf{k})}{4 \sum_{i=1}^3 \sin^2(k_i/2)} . \quad (10)$$

The smearing factor $S_{\text{HYP}}(\mathbf{k})$ is detailed in [50]. The correction term allows for a perfect fit, even including the $r = 1$ value, see Fig. 9. Actually, as observed by other authors, the result lies very close to what one gets when fitting only the continuum shape of the potential to a restricted range $2 \leq r \leq 7$.

From the resulting potential without the correction term ΔV and the condition

$$r^2 \left. \frac{dV(r)}{dr} \right|_{r=r_0} = 1.65 , \quad (11)$$

we obtain the Sommer parameter in lattice units,

$$r_0 = \sqrt{\frac{1.65 + B}{\sigma}} = \frac{r_{0,\text{exp}}}{a} . \quad (12)$$

The lattice spacing is thus given by $a = r_{0,\text{exp}}/r_0$. Using $r_{0,\text{exp}} = 0.48$ fm, our values for the lattice spacing are given in Table IV.

Run	a [fm]	$a/r_{0,\text{exp}}$	$a m_{\text{AWI}}$	m_{AWI} [MeV]
A	0.1507(17)	0.3139(35)	0.0327(3)	42.8(4)
B	0.1500(12)	0.3126(24)	0.0259(2)	34.1(2)
C	0.1440(12)	0.3000(24)	0.0111(2)	15.3(3)

TABLE IV: Lattice spacing as defined via the Sommer parameter and AWI-mass in lattice units and in physical units via that scale setting.

The physical value of $r_{0,\text{exp}}$ for our situation (two mass degenerate quarks) is not accessible. Often the scale is set by extrapolating the measured values of the lattice spacing to vanishing quark mass and using the extrapolated value for all mass values [52] (mass independent scheme). In the present state of our simulations we have only one mass value for each gauge coupling. We therefore rely on the mass dependent definition, which differs by $\mathcal{O}(a)$ corrections. We also could use the nucleon mass to set the scale. In some of the mass plots shown below we therefore plot the masses in units of the nucleon mass.

B. The axial Ward identity mass

Another important observable in lattice QCD calculations is the (unrenormalized) quark mass from the axial Ward identity and the PCAC relation, the so-called AWI-mass (or PCAC-mass). Therefore, we compute the ratio

$$m_{\text{AWI}} = \frac{1}{2} \frac{c_A}{c_P} \frac{\langle \partial_t A_4(\vec{p}=0, t) P(0) \rangle}{\langle P(\vec{p}=0, t) P(0) \rangle}. \quad (13)$$

Both interpolators

$$A_4 = \bar{d} \gamma_4 \gamma_5 u, \quad P = \bar{d} \gamma_5 u, \quad (14)$$

couple to the pseudoscalar meson channel (here, time is direction 4). In relating the lattice measurements to the $\overline{\text{MS}}$ -scheme, these operators are usually defined with point-like quark sources. The normalization factors c_A , c_P relate the smeared source lattice operators to the point source lattice operators,

$$c_X = \frac{\langle X^{(p)}(t) P^{(p)}(0) \rangle}{\langle X^{(s)}(t) P^{(p)}(0) \rangle}, \quad (15)$$

where the upper index (s) or (p) indicates smeared or point sources, respectively, and X refers to A_4 or P . The ratio c_A/c_P is read off from the plateau range as exhibited in Fig. 10 for the case of the wide sources.

For the ratio in Eq. (13) we need derivatives of the correlator with respect to t . We obtain the numerical derivatives from local 3-point fits to the expected cosh-behavior of the correlator, involving values at $(t-1, t, t+1)$.

In Fig. 10 we show the AWI-mass ratio Eq. (13) vs. t and give the corresponding numbers in Table IV. The values are symmetrized with regard to $T/2$ and the error is estimated by single elimination jackknife. To obtain the final value for m_{AWI} , the ratio was averaged from $t = 4, \dots, 16$, weighted according to the statistical errors.

To relate this lattice value of m_{AWI} to an $\overline{\text{MS}}$ -value (e.g., at $\mu=2$ GeV) we still need to extrapolate to the chiral limit and compute the corresponding renormalization constants of the axial and

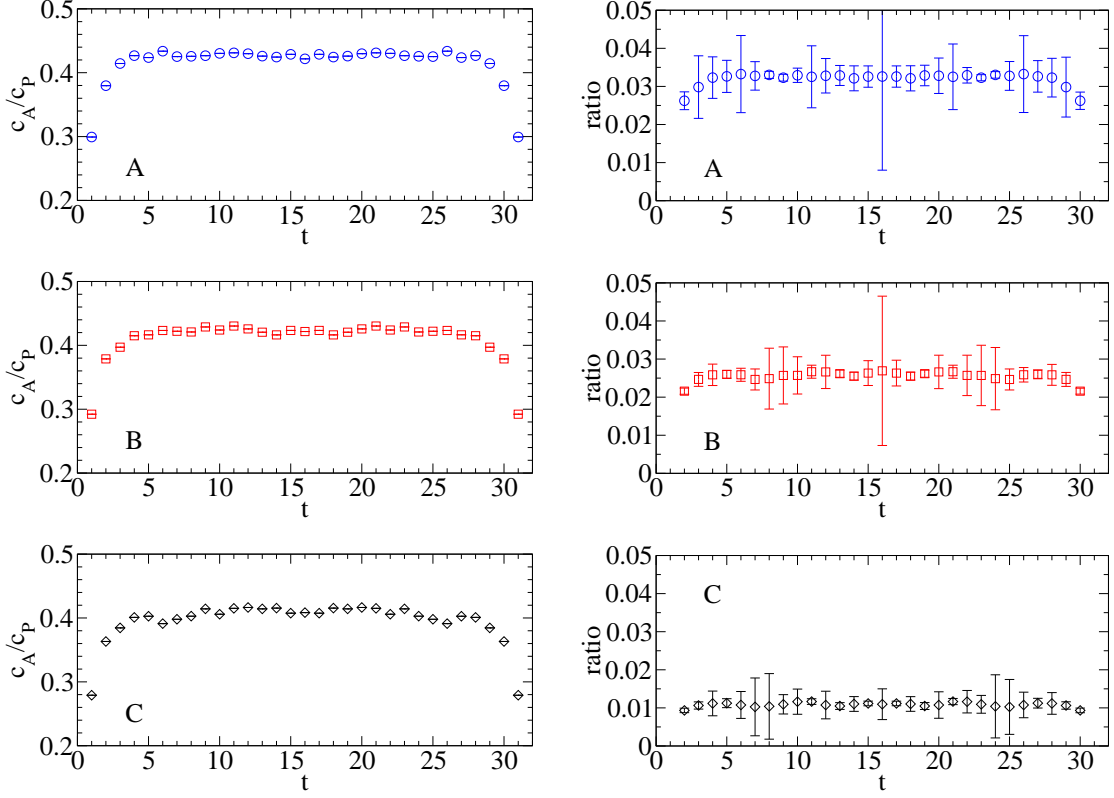


FIG. 10: L.h.s.: Ratio c_A/c_P for each run. R.h.s.: The AWI-mass ratios from Eq. (13) (runs A, B and C from top to bottom).

the pseudoscalar operators,

$$m_{\overline{\text{MS}}} = m_{\text{AWI}} Z_A / Z_P . \quad (16)$$

The Gell-Mann-Oakes-Renner (GMOR) relation establishes (in leading order in the quark mass) the connection between the pion mass m_π and the quark mass m , with F_π and Σ denoting the pion decay constant and the chiral condensate, respectively,

$$F_\pi^2 m_\pi^2 = -2 m \Sigma . \quad (17)$$

From Fig. 11 one sees that the expected linear dependence of m_π^2 on m_{AWI} is nicely reproduced. In addition to the three fully dynamical points we also show the partially quenched values, where the valence quark mass is larger than the sea quark mass. These points, including the partially quenched ones, are all compatible with a common behavior.

C. Pion decay constant

The pion decay constant F_π can be extracted from the correlator $\langle A_4 A_4 \rangle$ via

$$c_A^2 Z_A^2 \langle A_4(\vec{p} = 0, t) A_4(\vec{p} = 0, 0) \rangle \xrightarrow{\text{large } t} m_\pi F_\pi^2 e^{-m_\pi t} . \quad (18)$$

Here, we also use the normalization factor c_A from Eq. (15) in order to remove the dependence on the quark smearing. The axial vector lattice field operators have to be multiplied with normalization constants Z_A in order to ensure correct current conservation in the chiral limit. For the

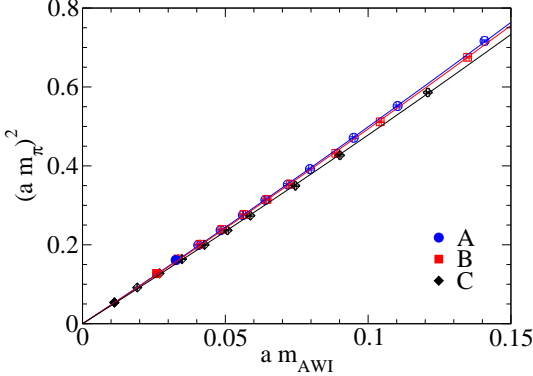


FIG. 11: Gell-Mann-Oakes-Renner plot for the three runs. Full symbols represent the fully dynamical points whereas open symbols are data points for which $m_{\text{val}} > m_{\text{sea}}$. The curves represent fits to $a m + b m^2$.

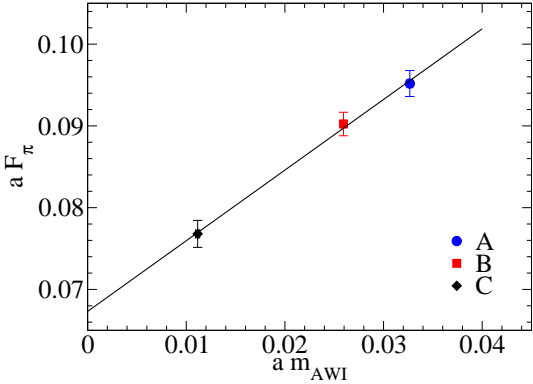


FIG. 12: F_π in lattice units with a linear fit to the three dynamical points. These values have not been corrected by multiplication with Z_A .

quenched results these were determined for D_{CI} in [24] resulting in values close to 1. In Fig. 12 we plot F_π vs. the AWI-mass.

IV. RESULTS FOR THE HADRON GROUND STATES

A. Spectrum analysis: Variational method

Over the last two decades lattice QCD has turned into a powerful tool for computing the mass spectrum of hadrons. Such a reproduction of experimental evidence from an ab-initio calculation is a strong test for the correctness of QCD. However, one mostly is restricted to the ground state masses, since excited state contributions only appear as sub-leading terms in the Euclidean correlators. Thus, a reliable separation of excited and ground states, but also of different excited states themselves, is a rather challenging enterprise.

Nowadays several different approaches towards that goal are used in hadron spectroscopy. One could do a brute-force least-squares fit to a finite sum of exponentials, but this is known to give conclusive results only if high statistics are available. Other methods are based on Bayesian fitting [53, 54, 55, 56, 57], subtractions [58] or evolutionary fitting methods [59, 60]. Here, however, we

use a different state-of-the-art approach, namely the variational method [47, 61] which has been used quite extensively within the BGR collaboration [62, 63, 64, 65, 66, 67, 68, 69, 70]. For a recent review on results for the variational method see [71].

In the variational method a matrix built from different correlators is used. These correlators contain interpolators with different Dirac structure and quarks smeared with different widths. Such a choice allows for a better overlap of the interpolating fields with the physical states. Given a set of N basis interpolators $O_i, i = 1, \dots, N$, we compute a matrix of cross correlations,

$$C_{ij}(t) = \langle O_i(t) \overline{O}_j(0) \rangle . \quad (19)$$

Considering the generalized eigenvalue problem, normalized at some time slice $t_0 < t$,

$$C(t) \cdot \vec{v}_k = \lambda_k(t, t_0) \cdot C(t_0) \cdot \vec{v}_k , \quad (20)$$

one can show along the lines of [61, 72], that the eigenvalues λ_k behave as

$$\lambda_k(t, t_0) \propto e^{-(t-t_0)m_k} \left[1 + \mathcal{O}(e^{-(t-t_0)\Delta m_k}) \right] . \quad (21)$$

In general, Δm_k is the mass difference to the closest lying state. For a more detailed discussion of the error terms see [72]. Each of the interpolators O_i has the quantum numbers of the corresponding hadron channel and is projected to a certain spatial momentum, which is always zero in our case. For all considered hadron channels we use $t_0 = 1$.

For a sufficiently large set of basis interpolators each eigenstate decays exponentially with its energy according to Eq. (21). The eigenstate with slowest decay (i.e., the largest eigenvalue) corresponds to the ground state, the second largest to the first excited state, and so on. We now can fit the states by stable two parameter fits of the eigenvalues in a range of t -values where the correlator is dominated by a single exponential. In order to identify the corresponding range for the fit we analyze effective masses for the eigenvalues,

$$m_k^{(\text{eff})}(t + 1/2) = \ln \left(\frac{\lambda_k(t)}{\lambda_k(t + 1)} \right) . \quad (22)$$

For sufficiently large values of t the effective masses form plateaus, which then give us the range for the fit.

Another important instrument to estimate the quality of the signal are the eigenvectors \vec{v}_k of Eq. (20), acting as fingerprints for each state. The components also should show a plateau behavior with regard to the correlation distance where the channel is dominated by a single state. Thus, the fits of the eigenvalues should only be performed in a t -range where both effective masses and eigenvectors show a reliable plateau.

B. Jacobi smearing of quark sources

Hadron correlation functions are built from quark propagators D^{-1} acting on some quark source S . In order to improve the signal and to extend the operator basis we work with extended sources obtained by Jacobi smearing [73, 74]: A point-like source S_0 is smeared out by acting with a smearing operator M ,

$$S = M S_0 , \quad M = \sum_{n=0}^N (\kappa H)^n , \quad (23)$$

Meson	J^{PC}	Number	Operator
Pseudoscalar	0^{+-}	1	$\bar{u}_n \gamma_5 d_n$
		2	$\bar{u}_n \gamma_5 d_w$
		3	$\bar{u}_w \gamma_5 d_w$
		4	$\bar{u}_n \gamma_t \gamma_5 d_n$
		5	$\bar{u}_n \gamma_t \gamma_5 d_w$
		6	$\bar{u}_w \gamma_t \gamma_5 d_w$
Vector	1^{--}	1	$\bar{u}_n \gamma_k d_n$
		2	$\bar{u}_n \gamma_k d_w$
		3	$\bar{u}_w \gamma_k d_w$
		4	$\bar{u}_n \gamma_k \gamma_t d_n$
		5	$\bar{u}_n \gamma_k \gamma_t d_w$
		6	$\bar{u}_w \gamma_k \gamma_t d_w$

TABLE V: Meson interpolators used in this study. We use $\gamma_t = \gamma_4$, i.e., the 4-direction corresponds to the Euclidean time direction. The subscripts n or w denote the narrow or wide smeared quark source.

where H is a hopping term,

$$H = \sum_{j=1}^3 \left[U_j(\vec{x}, t) \delta_{\vec{x}+\hat{j}, \vec{y}} + U_j^\dagger(\vec{x} - \hat{j}, t) \delta_{\vec{x}-\hat{j}, \vec{y}} \right]. \quad (24)$$

The smearing extends only over individual time slices, i.e., t is fixed. The parameters κ (hopping parameter) and N (number of smearing steps) are tuned to get an approximately Gaussian shape of the quark source with a certain width. We use the values for κ and N given in [68] for the $16^3 \times 32$ lattice to obtain a narrow (index n) and a wide (index w) source.

C. Hadron interpolators

Working with the variational method one strives for a good basis of interpolators O_i from which one can obtain a combination coupling strongly to the hadron of interest. These interpolators should simultaneously be linearly independent, as orthogonal as possible and sufficient to represent the physical states reasonably well. Thus, the crucial point is the design of different interpolators.

A complete list of our meson interpolators can be found in Tab. V. All considered interpolators represent isovector ($I = 1$) mesons.

Interpolators for baryons are slightly more complicated since there are three quarks involved. The general form of a local interpolator for the nucleon is given by

$$O_N = \epsilon_{abc} \Gamma_1 u_a (u_b^T \Gamma_2 d_c - d_b^T \Gamma_2 u_c), \quad (25)$$

where a, b, c are color indices and Γ_1, Γ_2 are combinations of γ -matrices. In Tab. VI the different possibilities are listed.

The delta baryon has a simpler structure, since there only one Dirac structure is analyzed. Its interpolator has the following form,

$$O_{\Delta,k} = \epsilon_{abc} u_a (u_b^T C \gamma_k u_c), \quad k = 1, 2, 3. \quad (26)$$

We project this to spin $\frac{3}{2}$ and average the correlators as discussed in [69].

Γ_1	Γ_2	Number	Smearing
$\mathbb{1}$	$C\gamma_5$	1	$n(nn)$
		2	$n(nw)$
		3	$n(wn)$
		4	$n(ww)$
		5	$w(wn)$
		6	$w(ww)$
$i\mathbb{1}$	$C\gamma_4\gamma_5$	13	$n(nn)$
		14	$n(nw)$
		15	$n(wn)$
		16	$n(ww)$
		17	$w(wn)$
		18	$w(ww)$

TABLE VI: Nucleon $I(J^P) = \frac{1}{2} \left(\frac{1}{2}^+\right)$ interpolators. The reference numbers of the interpolators are chosen to be consistent with earlier publications [68, 69].

Number	Smearing
1	$n(nn)$
2	$n(nw)$
3	$n(wn)$
4	$n(ww)$
5	$w(wn)$
6	$w(ww)$

TABLE VII: Delta baryon $I(J^P) = \frac{3}{2} \left(\frac{3}{2}^+\right)$ interpolators. The reference numbers of the interpolators are chosen to be consistent with earlier publications [68, 69].

We introduce a short-hand notation for the different baryon interpolators. We denote them by $s_1(s_2s_3)$, where s_i represents the smearing type of quark i ; e.g., in $n(ww)$ the first quark has a narrow smearing, the second and third have wide smearings. The interpolators for the baryons studied here can be found in Tables VI and VII. All baryon correlators are projected to definite parity.

For subsequent configurations the quark sources (and thus the hadron interpolators) are placed at alternating positions $d_i = (t, \vec{x})$ with

$$\begin{aligned}\vec{d}_1 &= (0, 0, 0, 0), \\ \vec{d}_2 &= (16, 0, 0, 0), \\ \vec{d}_3 &= (0, 8, 8, 8), \\ \vec{d}_4 &= (16, 8, 8, 8),\end{aligned}\tag{27}$$

in order to get better statistical decorrelation of the data. All hadron interpolators are projected to vanishing spatial momentum.

Meson	Interpolator(s)	Run	Fit range	Mass [MeV]
Pseudoscalar	3	A	4–15	526(7)
		B	4–15	469(4)
		C	5–15	318(5)
Vector	4,5,6	A	3–10	922(17)
		B	3–13	897(13)
		C	4–9	810(28)

TABLE VIII: Here we show the interpolators entering the final analysis and the best fit ranges for the different runs. We also give the resulting mass values using the lattice spacing given in Table IV.

D. Effective masses and fit ranges

Only a posteriori one can judge on the amount of independence of the interpolators used. Including too many interpolators in the correlation matrix increases the statistical noise in the diagonalization. Our aim is to get the best signal in each channel and this is obtained by having the best plateaus in the effective masses. We therefore, after studying the quality of results with different subsets of interpolators, decided on as few of them as seemed sufficient for a stable signal. For example, for the positive parity nucleon we only included the interpolators 4–6 and 16–18. The optimal selection may be different when we study higher excitations and may include differently smeared quark sources.

E. The meson sector

Since we simulate two mass-degenerate light quarks, interpolators of the form $\bar{u}_n \Gamma d_w$ and $\bar{u}_w \Gamma d_n$ are identical. Tab. V lists the interpolators used. Due to the two different possibilities for Γ we have for the pseudoscalar and vector particle six interpolators at hand. Only a subset of these is used for the final analysis.

We restricted ourselves to fit only plateaus with three or more consecutive points. In addition to that we started fits only at points for which $t - t_0 \geq 2$. Table VIII gives the information on the interpolators and the fit ranges used in the final analysis.

1. The pseudoscalar meson

Let us start our discussion with the particle where the best signal can be extracted, the pseudoscalar meson ($J^{PC} = 0^{-+}$). For the determination of the ground state we used one interpolator (no. 3) and performed a cosh-fit.

Fig. 13 demonstrates a peculiarity of the generalized eigenvalue problem, as it was observed already in, e.g., Refs. [70, 75]. On the periodically closed lattice mesons propagate forward and backward in time. An interpolator which couples to a particular state at small t will also couple to the same, but backward running, state at high t . In the standard eigenvalue problem, depending on the time extent and the masses of ground state and excited state, above some value of $0 < t_1 \leq n_t/2$ the backward running ground state will have a larger eigenvalue than the first excited state. In that region of t -values the second largest eigenvalue increases towards $n_t/2$. In the generalized eigenvalue problem the eigenvalues are all normalized to unity at timeslice t_0 . Thus the second largest eigenvalue signal is shifted upwards and the upwards increasing eigenvalue discussed may

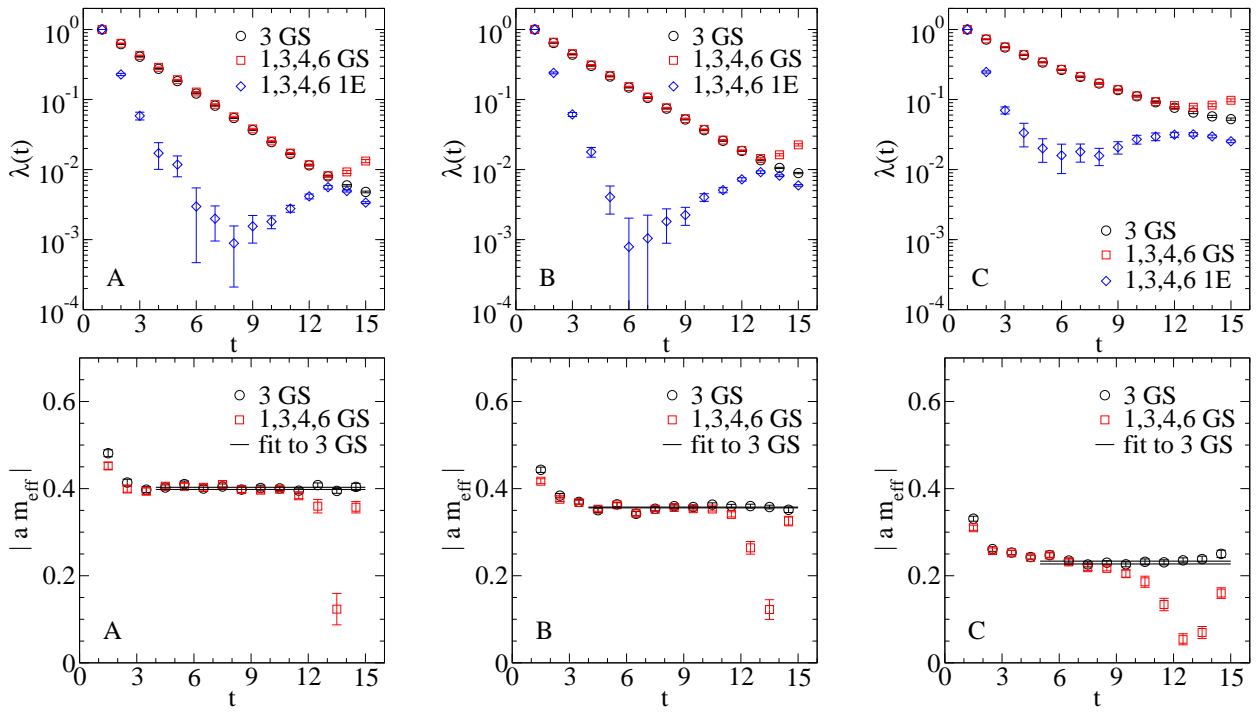


FIG. 13: In the first row the eigenvalues for the pseudoscalar channel ($J^{PC} = 0^{-+}$) are shown (runs A, B, C from left to right). In each plot we show data for two different sets of interpolators: Circles represent the ground state using interpolator 3, squares and diamonds show the ground state (GS) and the first excited state (1E) using the interpolator set 1, 3, 4, 6, respectively (numbers according to Tab. V). In the second row the absolute value of the corresponding effective masses (in lattice units) of the ground states are plotted as a function of t . The horizontal line indicates the fit range and mass value obtained by the fit of the ground state eigenvalue of interpolator 3 over the specified range.

now even becomes at some value t_2 larger than the eigenvalue of the ground state. This behavior is observed in Fig. 13 where we plot the first two eigenvalues of the pseudoscalar state resulting from the generalized eigenvalue problem analysis. For our choice of $t_0 = 1$ the (in time) backward running ground state becomes the second largest eigenvalue near $t_1 = 6$ and the largest eigenvalue near $t_2 = 13$. Near the crossing this leads to a misidentification (the real ground state signal becomes the second largest eigenvalue) which explains the bump in the effective mass $|am_{\text{eff}}|$.

These properties can be seen very nicely in the 2-dimensional model of [76]. This behavior of the eigenvalues is a fundamental feature of the variational method; the signals of ground and excited states are disentangled up to that point in time where these signals are crossing with the lightest backward running state. The larger the difference in the ground and excited states, the earlier this crossing takes place.

For simplicity, and since the results for the corresponding plateau regions agree within errors, we choose the single correlator value where we find the longest plateau. In Fig. 13 we compare the effective masses of the ground states for two different choices of interpolators. One can clearly see that the two sets of effective masses can be fitted reliably in an appropriate region.

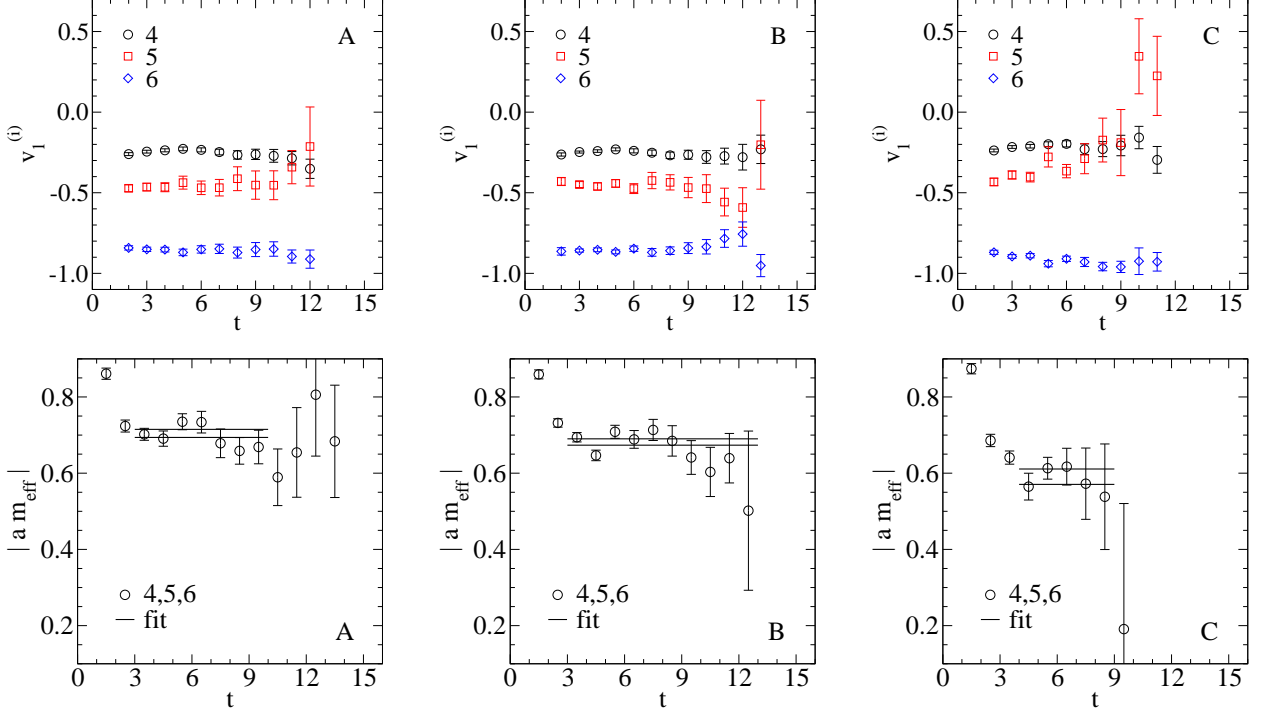


FIG. 14: In the first row the normalized eigenvector components of the ground state $v_1^{(i)}$, $i = 4, 5, 6$, of the vector meson ($J^{PC} = 1^{--}$) are plotted against the time distance t . From left to right we show runs A, B and C. In the second row the effective masses of the vector meson (in lattice units) are plotted as a function of t . The solid black lines indicate our fit range of the fit to the corresponding leading eigenvalue and the upper and lower bound of the extracted value. Also here, from left to right we show runs A, B and C.

2. The vector meson

In the case of the vector meson we can take the eigenvector components as a tool to determine fit ranges (cf., Table VIII). The interpolators we included in the correlation matrix are no. 4, 5, 6. In Fig. 14 we plot the eigenvector components and effective mass of the ground state. One can see from the plots that the quality of the data is sufficient to make a fit, but it is not as good as for the pion.

On the l.h.s. of Fig. 15 we plot the fitted mass against m_π^2 . The scale is set by the lattice spacing of Table IV. Within error bars, all three runs agree nicely with each other and run C extrapolates close to the experimental value.

As discussed in Sect. III we set the scale by assuming as Sommer parameter value of 0.48 fm for all three runs. In the r.h.s. of Fig. 15 we use the scale of the nucleon mass instead. Here the data of run B seem to be somewhat higher than runs A and C.

We emphasize that the physical ρ is a resonance and that multiple lattice volumes would be needed for a thorough analysis.

F. The baryon sector

In this presentation we restrict ourselves to baryons with positive parity. A more detailed analysis, also including excited states, is in progress. The definitions for the nucleon and delta baryons were given earlier in Eqs. (25) and (26). Details of the interpolators used can be found in

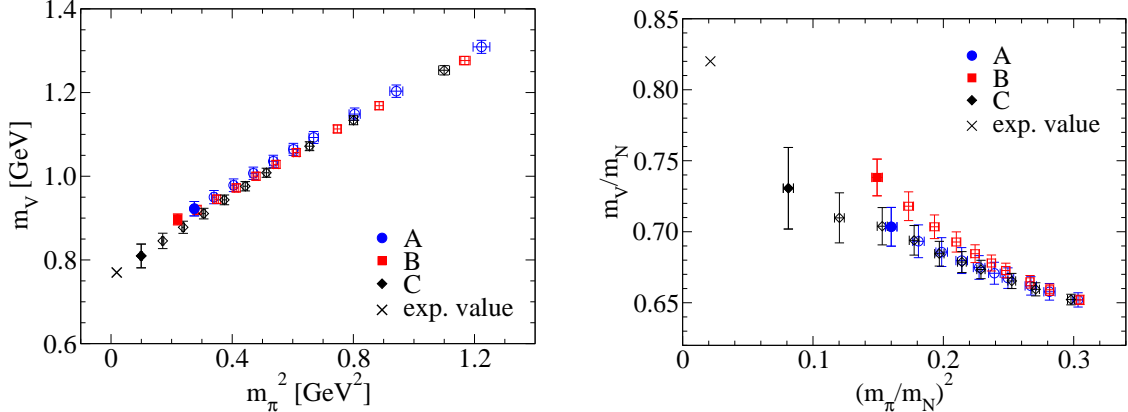


FIG. 15: L.h.s.: The vector meson mass m_V is plotted against the pseudoscalar mass m_π^2 . R.h.s.: An APE plot (scaled by the nucleon mass m_N). Both plots show the fully dynamical data (filled symbols) and the partially quenched dynamical data (open symbols) for runs A, B, C. The physical point is marked with a black cross.

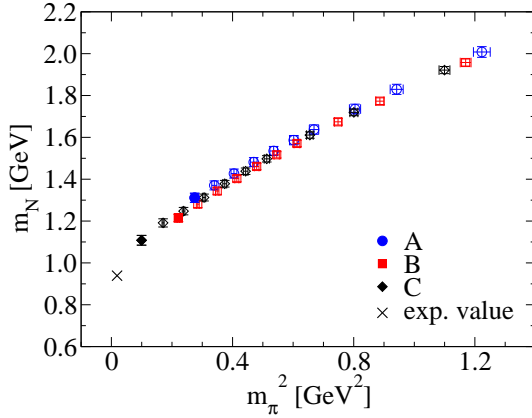


FIG. 16: The (positive parity) nucleon mass m_N is plotted against the pseudoscalar mass m_π^2 for the fully dynamical data (filled symbols) and for the partially quenched dynamical data (open symbols) for runs A, B, C. The experimental value is marked with a black cross.

Tables VI and VII.

1. The nucleon

For the diagonalization process we used the interpolators 4, 5, 6, 16, 17, 18 according to Tab. VI. The results are shown in Fig. 16. All of the data sets extrapolate towards the physical point.

2. The delta resonance

For the Δ resonance we have a set of 6 different interpolators at hand (see Tab. VII) and in principle we can allow for $2^6 - 1 = 63$ combinations. All these combinations give rise to reasonable fit results. In the end we used the combination 1, 2, 4, 5, 6, see Fig. 17. However, a naive (linear in

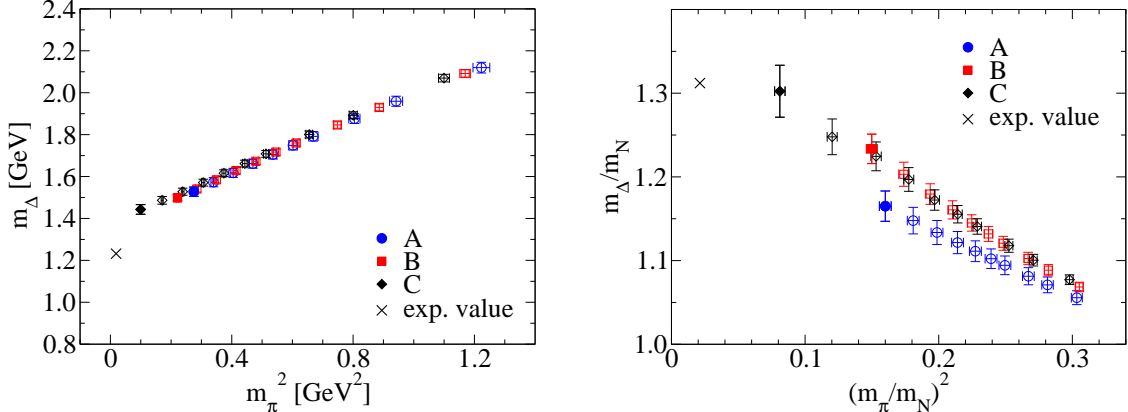


FIG. 17: L.h.s.: The (positive parity) delta baryon mass m_Δ is plotted against the pseudoscalar mass m_π^2 . R.h.s.: An APE plot (scaled by the nucleon mass) for the dynamical runs A, B, C. Both plots show the fully dynamical data (filled symbols) and the partially quenched dynamical data (open symbols) for runs A, B, C. The physical point is marked with a black cross.

Baryon	Interpolator(s)	Run	Fit range	Mass [MeV]
Nucleon (pos. parity)	4,5,6,16,17,18	A	3–11	1311(22)
		B	4–11	1215(18)
		C	3–8	1108(23)
Delta (pos. parity)	1,2,4,5,6	A	3–6	1528(22)
		B	3–6	1498(15)
		C	3–6	1443(23)

TABLE IX: Interpolators and fit ranges used for the baryon ground states. The mass values are obtained using the lattice spacing given in Table IV.

m_π^2) extrapolation overestimates the physical value by about 10% - 15%. On the r.h.s. of Fig. 17 we show an APE plot, scaled by the nucleon mass. One may argue that in this plot some finite size artefacts cancel such that the extrapolation to the physical point is improved.

V. SUMMARY AND CONCLUSIONS

In this paper we presented first results from dynamical simulations with CI fermions on lattices of size $16^3 \times 32$ with spatial extent of 2.4 fm. After detailing the technical aspects of our simulation we showed that so-called exceptional configurations are suppressed in simulations with CI fermions. This enables us to simulate at pion masses of roughly 320 MeV on rather coarse lattices. We observe frequent tunneling between topological sectors and reasonably small autocorrelation times.

As a first physical application we presented results for the pion decay constant F_π and for the ground state masses of selected mesons and baryons. While scale setting remains an issue with dynamical simulations, the results from all three runs are consistent and naive extrapolations of our data are also consistent with experiment. Further simulations at different lattice spacings and in larger volumes will be needed in order to control the effects of the lattice discretization and to estimate the finite volume corrections, thereby making closer contact with experimental results.

We are currently improving the basis for the variational method and investigating the effects of

quark and link smearing on the quality of excited state signals, thus providing a systematic study of excited meson and baryon states for a larger set of quantum numbers.

Acknowledgments

We are grateful to Meinulf Göckeler for discussions. We also thank T. Maurer for help in an earlier stage of this work. The calculations have been performed on the SGI Altix 4700 of the Leibniz-Rechenzentrum Munich and on local clusters at ZID at the University of Graz. We thank these institutions for providing support. M.L. and D.M. are supported by “Fonds zur Förderung der wissenschaftlichen Forschung in Österreich” (DK W1203-N08). C.H. and A.S. acknowledge support by DFG and BMBF. The work has been supported by DFG project SFB/TR-55.

APPENDIX A: CI OPERATOR AND LÜSCHER-WEISZ GAUGE ACTION

1. The CI operator

Throughout the dynamical simulations we used the CI Dirac operator introduced in [9, 10, 77]. The coefficients multiply terms of the action according to the definition in

$$D = m_0 \mathbb{1} + D_{\text{CI}}, \quad D_{\text{CI}}(n, m) = \sum_{i=1}^{16} c_{nm}^{(i)}(U) \Gamma_i, \quad (\text{A1})$$

where the sum runs over all 16 elements Γ_i of the Clifford algebra. To each element we assign a coefficient $c_{nm}^{(i)}$, consisting of sums of path ordered products of the link variables U which connect the lattice sites n and m . Plugging this ansatz into the Ginsparg-Wilson equation leads to a set of algebraic equations, which can be solved to obtain D_{CI} . Additional restrictions come from the lattice symmetries and γ_5 -hermiticity. The solution can in principle be exact if one allows for an infinite number of terms. For practical reasons the number of terms is finite and thus the solution is a truncated series solution of the Ginsparg-Wilson relation. In our simulation paths up to length four are used, given in Table X.

2. The Lüscher-Weisz gauge action

The Lüscher-Weisz gauge action [29] is given by

$$S_g = -\beta_1 \sum_{\text{pl}} \frac{1}{3} \text{Re} \text{tr} U_{\text{pl}} - \beta_2 \sum_{\text{re}} \frac{1}{3} \text{Re} \text{tr} U_{\text{re}} - \beta_3 \sum_{\text{tb}} \frac{1}{3} \text{Re} \text{tr} U_{\text{tb}}, \quad (\text{A2})$$

where U_{pl} is the usual Wilson plaquette, U_{re} is a planar (2×1)-plaquette and U_{tb} is a closed loop of length 6 along the edges of a 3-cube (“twisted bent”). Here, β_1 is the independent gauge coupling and the two other couplings are determined from tadpole-improved perturbation theory [78]. With

$$u_0 = \left(\frac{1}{3} \text{Re} \text{Tr} \langle U_{\text{pl}} \rangle \right)^{1/4}, \quad \alpha = -\frac{1}{3.06839} \log u_0^4, \quad (\text{A3})$$

we get for β_2, β_3 the following expressions,

$$\beta_2 = \frac{\beta_1}{20u_0^2} (1 + 0.4805\alpha), \quad \beta_3 = \frac{\beta_1}{u_0^2} 0.03325\alpha. \quad (\text{A4})$$

Coeff. number	Name	Value	Path shape	γ	Multiplicity
1	s_1	1.481599252	[]	1	1
2	s_2	-0.05218251439	[i]	1	8
3	s_3	-0.01473643847	[i, j]	1	48
5	s_5	-0.002186103421	[i, j, k]	1	192
6	s_6	0.002133989696	[i, i, j]	1	96
8	s_8	-0.003997001821	[i, j, -i]	1	48
10	s_{10}	-0.0004951673735	[i, j, k, l]	1	384
11	s_{11}	-0.0009836500799	[i, j, -i, k]	1	384
13	s_{13}	0.007529838581	[i, j, -i, -j]	1	48
14	v_1	0.1972229309	[i]	γ_i	8
15	v_2	0.008252157565	[i, j]	γ_i	96
17	v_4	0.005113056314	[i, j, k]	γ_i	384
18	v_5	0.001736609425	[j, i, k]	γ_i	192
32	t_1	-0.08792744664	[i, j]	$\gamma_i \gamma_\nu$	48
33	t_2	-0.002553055577	[i, j, k]	$\gamma_i \gamma_j$	384
34	t_3	0.002093792069	[i, k, j]	$\gamma_i \gamma_j$	192
36	t_5	-0.005567377075	[i, j, -i]	$\gamma_i \gamma_j$	48
46	t_{15}	-0.003427310798	[j, i, -j, -i]	$\gamma_i \gamma_j$	48
51	p_1	-0.008184103136	[i, j, k, l]	γ_5	384

TABLE X: Coefficients for the CI fermion action used in this simulation. The path shapes are given symbolically, e.g., $[i, j]$ stands for a path in i -direction and then in j -direction ($i \neq j$). The γ -matrices (5-th column) are also permuted as described in more detail in [10].

By u_0 in Eq. (A3) we denote the assumed plaquette, $\text{Re} \text{Tr} \langle U_{\text{pl}} \rangle$, thus the coefficients have to be calculated self-consistently.

-
- [1] P. H. Ginsparg and K. G. Wilson, Phys. Rev. D **25**, 2649 (1982).
 - [2] M. Lüscher, Phys. Lett. B **428**, 342 (1998), hep-lat/9802011.
 - [3] H. Neuberger, Phys. Lett. B **417**, 141 (1998), hep-lat/9707022.
 - [4] H. Neuberger, Phys. Lett. B **427**, 353 (1998), hep-lat/9801031.
 - [5] D. B. Kaplan, Phys. Lett. B **288**, 342 (1992), hep-lat/9206013.
 - [6] V. Furman and Y. Shamir, Nucl. Phys. **B439**, 54 (1995), hep-lat/9405004.
 - [7] P. Hasenfratz and F. Niedermayer, Nucl. Phys. **B414**, 785 (1994), hep-lat/9308004.
 - [8] A. Hasenfratz, P. Hasenfratz, and F. Niedermayer, Phys. Rev. D **72**, 114508 (2005), hep-lat/0506024.
 - [9] C. Gatringer, Phys. Rev. D **63**, 114501 (2001), hep-lat/0003005.
 - [10] C. Gatringer, I. Hip, and C. B. Lang, Nucl. Phys. **B597**, 451 (2001), hep-lat/0007042.
 - [11] T. Kaneko, S. Aoki, H. Fukaya, S. Hashimoto, K.-I. Ishikawa, K. Kanaya, H. Matsufuru, M. Okamoto, M. Okawa, T. Onogi, et al., PoS **LAT2006**, 054 (2006), hep-lat/0610036.
 - [12] H. Matsufuru, H. Fukaya, S. Hashimoto, K. Kanaya, T. Kaneko, K. Ogawa, M. Okamoto, T. Onogi, and N. Yamada, PoS **LAT2006**, 031 (2006), hep-lat/0610026.
 - [13] S. Aoki, H. Fukaya, S. Hashimoto, K.-I. Ishikawa, K. Kanaya, T. Kaneko, H. Matsufuru, M. Okamoto, M. Okawa, T. Onogi, et al. (2008), arXiv:0803.3197 [hep-lat].
 - [14] J. Noaki, S. Aoki, H. Fukaya, S. Hashimoto, T. Kaneko, H. Matsufuru, T. Onogi, E. Shintani, and N. Yamada, PoS **LATTICE 2007**, 126 (2007), arXiv:0710.0929 [hep-lat].
 - [15] N. Cundy, S. Krieg, and T. Lippert, PoS **LAT2005**, 107 (2005), hep-lat/0511044.

- [16] N. Cundy, S. Krieg, G. Arnold, A. Frommer, T. Lippert, and K. Schilling (2005), hep-lat/0502007.
- [17] N. Cundy, S. Krieg, T. Lippert, and A. Schäfer, PoS **LATTICE2007**, 030 (2007), arXiv:0710.1785 [hep-lat].
- [18] N. Cundy, S. Krieg, T. Lippert, and A. Schäfer (2008), arXiv:0803.0294 [hep-lat].
- [19] T. DeGrand and S. Schaefer, Phys. Rev. D **71**, 034507 (2005), hep-lat/0412005.
- [20] T. DeGrand and S. Schaefer, Phys. Rev. D **72**, 054503 (2005), hep-lat/0506021.
- [21] Z. Fodor, S. D. Katz, and K. K. Szabo, Nucl. Phys. B (Proc. Suppl.) **140**, 704 (2005), hep-lat/0409070.
- [22] G. I. Egri, Z. Fodor, S. D. Katz, and K. Szabo, JHEP **0601**, 049 (2006), hep-lat/0510117.
- [23] C. Gattringer, M. Göckeler, P. Hasenfratz, S. Hauswirth, K. Holland, T. Jörg, K. J. Juge, C. B. Lang, F. Niedermayer, P. E. L. Rakow, et al., Nucl. Phys. **B677**, 3 (2004), hep-lat/0307013.
- [24] C. Gattringer, P. Huber, and C. B. Lang, Phys. Rev. D **72**, 094510 (2005), hep-lat/0509003.
- [25] C. B. Lang, P. Majumdar, and W. Ortner, Phys. Rev. D **73**, 034507 (2006), hep-lat/0512014.
- [26] R. Frigori, C. Gattringer, C. B. Lang, M. Limmer, T. Maurer, D. Mohler, and A. Schäfer, PoS **LATTICE2007**, 114 (2007), arXiv:0709.4582v1 [hep-lat].
- [27] C. B. Lang, Prog. Part. Nucl. Phys. **61**, 35 (2008), arXiv:0711.3091 [nucl-th].
- [28] C. B. Lang, P. Majumdar, and W. Ortner, PoS **LAT2005**, 131 (2005), hep-lat/0509005.
- [29] M. Lüscher and P. Weisz, Commun. Math. Phys. **97**, 59 (1985).
- [30] S. Dürr and C. Hoelbling, Phys. Rev. D **69**, 034503 (2004), hep-lat/0311002.
- [31] A. Hasenfratz and F. Knechtli, Phys. Rev. D **64**, 034504 (2001).
- [32] C. Morningstar and M. Peardon, Phys. Rev. D **69**, 054501 (2004), hep-lat/0311018.
- [33] A. Hasenfratz, R. Hoffmann, and S. Schaefer, JHEP **0705**, 029 (2007).
- [34] S. Dürr (2007), arXiv:0709.4110 [hep-lat].
- [35] S. Duane, A. D. Kennedy, B. J. Pendleton, and D. Roweth, Phys. Lett. B **195**, 216 (1987).
- [36] W. Ortner, Ph.D. thesis, Univ. Graz (2006).
- [37] M. Hasenbusch, Phys. Lett. B **519**, 177 (2001), hep-lat/0107019.
- [38] R. C. Brower, T. Ivanenko, A. R. Levi, and K. N. Orginos, Nucl. Phys. **B484**, 353 (1997), hep-lat/9509012.
- [39] S. Dürr, Z. Fodor, C. Hoelbling, R. Hoffmann, S. Katz, S. Krieg, T. Kurth, L. Lellouch, T. Lippert, K. Szabo, et al. (2008), arXiv:0802.2706 [hep-lat].
- [40] M. Creutz, Phys. Rev. D **38**, 1228 (1988).
- [41] Y. Namekawa, S. Aoki, M. Fukugita, K.-I. Ishikawa, N. Ishizuka, Y. Iwasaki, K. Kanaya, T. Kaneko, Y. Kuramashi, V. I. Lesk, et al., Phys. Rev. D **70**, 074503 (2004), hep-lat/0404014.
- [42] B. Joo, B. Pendleton, A. D. Kennedy, A. C. Irving, J. C. Sexton, S. M. Pickles, and S. P. Booth, Phys. Rev. D **62**, 114501 (2000), hep-lat/0005023.
- [43] S. Gupta, A. Irback, F. Karsch, and B. Petersson, Phys. Lett. B **242**, 437 (1990).
- [44] M. Atiyah and I. M. Singer, Ann. Math. **93**, 139 (1971).
- [45] R. Sommer, Nucl. Phys. **B411**, 839 (1994), hep-lat/9310022.
- [46] C. B. Lang and C. Rebbi, Phys. Lett. **115B**, 137 (1982).
- [47] C. Michael, Nucl. Phys. **B259**, 58 (1985).
- [48] R. G. Edwards, U. M. Heller, and T. R. Klassen, Nucl. Phys. **B517**, 377 (1998), hep-lat/9711003.
- [49] C. R. Allton, S. P. Booth, K. C. Bowler, J. Garden, A. Hart, D. Hepburn, A. C. Irving, B. Joó, R. D. Kenway, C. M. Maynard, et al., Phys. Rev. D **65**, 054502 (2002), hep-lat/0107021.
- [50] A. Hasenfratz, R. Hoffmann, and F. Knechtli, Nucl. Phys. B (Proc. Suppl.) **106**, 418 (2002), hep-lat/0110168.
- [51] C. Gattringer, R. Hoffmann, and S. Schaefer, Phys. Rev. D **65**, 094503 (2002), hep-lat/0112024.
- [52] S. Aoki, Nucl. Phys. B (Proc. Suppl.) **94**, 3 (2001), hep-lat/0011074.
- [53] C. Michael, Phys. Rev. D **49**, 2616 (1994), hep-lat/9310026.
- [54] C. Michael and A. McKerrell, Phys. Rev. D **51**, 3745 (1995), hep-lat/9412087.
- [55] M. Asakawa, T. Hatsuda, and Y. Nakahara, Prog. Part. Nucl. Phys. **46**, 459 (2001), hep-lat/0011040.
- [56] G. P. Lepage, B. Clark, C. T. H. Davies, K. Hornbostel, P. B. Mackenzie, C. Morningstar, and H. Trotter, Nucl. Phys. Proc. Suppl. **106**, 12 (2002), hep-lat/0110175.
- [57] Y. Chen, S.-J. Dong, T. Draper, I. Horváth, K.-F. Liu, N. Mathur, S. Tamhankar, C. Srinivasan, F. X. Lee, and J. Zhang (2004), hep-lat/0405001.
- [58] D. Guadagnoli, M. Papinutto, and S. Simula, Phys. Lett. B **604**, 74 (2004), hep-lat/0409011.
- [59] G. M. von Hippel, R. Lewis, and R. G. Petry, Comput. Phys. Commun. **178**, 713 (2008),

- arXiv:0707.2788 [hep-lat].
- [60] G. M. von Hippel, R. Lewis, and R. G. Petry, PoS **LATTICE2007**, 043 (2007), arXiv:0710.0014 [hep-lat].
 - [61] M. Lüscher and U. Wolff, Nucl. Phys. **B339**, 222 (1990).
 - [62] T. Burch, C. Gattringer, L. Y. Glozman, R. Kleindl, C. B. Lang, and A. Schäfer, Phys. Rev. D **70**, 054502 (2004), hep-lat/0405006.
 - [63] T. Burch, C. Gattringer, L. Y. Glozman, R. Kleindl, C. B. Lang, and A. Schäfer, Nucl. Phys. B (Proc. Suppl.) **140**, 284 (2005), hep-lat/0409014.
 - [64] T. Burch, C. Gattringer, L. Y. Glozman, C. Hagen, D. Hierl, C. B. Lang, and A. Schäfer, PoS **LAT2005**, 75 (2005), hep-lat/0509051.
 - [65] T. Burch, C. Gattringer, L. Y. Glozman, C. Hagen, D. Hierl, C. B. Lang, and A. Schäfer, PoS **LAT2005**, 097 (2005), hep-lat/0509086.
 - [66] T. Burch, C. Gattringer, L. Y. Glozman, C. Hagen, and C. B. Lang, Phys. Rev. D **73**, 017502 (2006), hep-lat/0511054.
 - [67] T. Burch, C. Gattringer, L. Y. Glozman, R. Kleindl, C. B. Lang, and A. Schäfer, Nucl. Phys. **A755**, 481 (2005), nucl-th/0501025.
 - [68] T. Burch, C. Gattringer, L. Y. Glozman, C. Hagen, C. B. Lang, and A. Schäfer, Phys. Rev. D **73**, 094505 (2006), hep-lat/0601026.
 - [69] T. Burch, C. Gattringer, L. Y. Glozman, C. Hagen, D. Hierl, C. B. Lang, and A. Schäfer, Phys. Rev. D **74**, 014504 (2006), hep-lat/0604019.
 - [70] C. Gattringer, L. Y. Glozman, C. B. Lang, D. Mohler, and S. Prelovsek, Phys. Rev. D **78**, 034501 (2008), arXiv:0802.2020 [hep-lat].
 - [71] C. Morningstar (2008), arXiv:0810.4448 [hep-lat].
 - [72] B. Blossier, G. von Hippel, T. Mendes, R. Sommer, and M. DellaMorte, PoS **LATTICE2008**, 135 (2008), arXiv:0808.1017 [hep-lat].
 - [73] S. Güsken et al., Phys. Lett. B **227**, 266 (1989).
 - [74] C. Best et al., Phys. Rev. D **56**, 2743 (1997), hep-lat/9703014.
 - [75] A. C. Lichtl, PoS **LATTICE2007**, 118 (2007), arXiv:0711.4072 [hep-lat].
 - [76] J. Danzer and C. Gattringer, PoS **LAT2007**, 092 (2007), arXiv:0710.1711 [hep-lat].
 - [77] C. Gattringer, M. Göckeler, P. E. L. Rakow, S. Schaefer, and A. Schäfer, Nucl. Phys. **B618**, 205 (2001), hep-lat/0105023.
 - [78] M. Alford, W. Dimm, G. P. Lepage, G. Hockney, and P. B. Mackenzie, Phys. Lett. B **361**, 87 (1995), hep-lat/9507010.